

# Tuning Local Proton Flux in Yolk-Shell Cu@Cu<sub>2</sub>Se Nanoreactors to Enable Efficient Electrochemical Nitrate-Ammonia Conversion

**Qi Hu**

Shenzhen University

**Hongju Zheng**

Shenzhen University

**Xiaodeng Wang**

Chongqing University of Arts and Sciences

**Keru Gao**

Shenzhen University

**Lingren Mi**

Shenzhen University

**Jianyong Cao**

Shenzhen University

**Qihua Huo**

Shenzhen University

**Laiyong Xie**

Shenzhen University

**Hengpan Yang**

Shenzhen University

**Xiaoyan Chai**

Shenzhen University

**Xiangzhong Ren**

Shenzhen University

**Chuan-Xin He** (✉ [hecx@szu.edu.cn](mailto:hecx@szu.edu.cn))

Shenzhen University <https://orcid.org/0000-0002-2254-360X>

---

## Article

**Keywords:** nitrate reduction reaction, yolk-shell structures, tandem nanoreactors, water dissociation, proton transfer

**Posted Date:** October 29th, 2021

**DOI:** <https://doi.org/10.21203/rs.3.rs-1006532/v1>

**License:**  This work is licensed under a Creative Commons Attribution 4.0 International License.

[Read Full License](#)

---

# Abstract

Electrochemical nitrate ( $\text{NO}_3^-$ ) reduction reaction ( $\text{NO}_3^-$ RR) represents an ideal alternative for ammonia ( $\text{NH}_3$ ) generation. Despite recent success on the synthesis of Cu-based electrocatalysts, the kinetics of Cu-catalyzed  $\text{NO}_3^-$ RR is still greatly limited by the slow proton transfer rate since the large energy barrier for water dissociation. Here, we report the construction of a yolk-shell structure, comprising a Cu core and  $\text{Cu}_2\text{Se}$  shell that functions like the tandem nanoreactor. Specifically, the  $\text{Cu}_2\text{Se}$  shell with strong water dissociation ability can easily produce protons and then transfer to the Cu core for driving the reduction of  $\text{NO}_3^-$ . Intriguingly, the proton flux arriving to the Cu core can be well tuned by altering the void size of the yolk-structure, thereby enabling rapid proton transfer yet hindering the competitive hydrogen evolution. More importantly, operando Raman spectra reveal that the rapid proton transfer significantly promotes the hydrogenation of key intermediates for reducing the overall energy barrier of the  $\text{NO}_3^-$ RR. Consequently, the optimized yolk-shell structure enables highly selective and efficient  $\text{NO}_3^-$ RR with a large  $\text{NH}_3$  yield rate of  $0.94 \text{ mmol cm}^{-2} \text{ h}^{-1}$ . This work offers a fresh concept to boost the  $\text{NO}_3^-$ RR by tuning proton transfer rate.

## 1. Introduction

Ammonia ( $\text{NH}_3$ ) is not only an essential feedstock for the production of various important nitrogenous chemicals (i.e., urea and nitric acid) but also a promising energy carrier with a high energy density ( $4.3 \text{ kWh kg}^{-1}$ ). [1, 2] Although a preferable  $\text{NH}_3$  yield rate has been achieved through the Haber-Bosch route, this route requires high temperature and pressure to activate the extremely inert nitrogen ( $\text{N}_2$ ), leading to extensive energy consumption. [3] To this end, an electrochemical reduction strategy, namely  $\text{N}_2$  reduction reaction (NRR), was developed to generate  $\text{NH}_3$  under ambient conditions. [4–6] Despite significant achievements have made on the synthesis of robust electrocatalysts for boosting the NRR, the  $\text{NH}_3$  yield rate is still highly unsatisfied, two or three orders of magnitude smaller than the Haber–Bosch route. Such poor performance can be firstly attributed to the large bond energy of  $\text{N}\equiv\text{N}$  ( $941 \text{ kJ mol}^{-1}$ ), in conjunction with the low solubility of  $\text{N}_2$  in aqueous electrolyte. [7, 8] Therefore, exploration of other nitrogen-containing sources to substitute  $\text{N}_2$  is essential for achieving the pursuit of efficient  $\text{NH}_3$  electrosynthesis under ambient conditions.

Recently, the nitrate ( $\text{NO}_3^-$ ) reduction reaction ( $\text{NO}_3^-$ RR) has attracted worldwide interest due to the markedly decreased energy for breaking the  $\text{N}=\text{O}$  bond ( $204 \text{ kJ mol}^{-1}$ ) with respect to the  $\text{N}\equiv\text{N}$  bond. [9, 10] As a result, compared with the NRR, both the reaction kinetics and  $\text{NH}_3$  yield rate are enhanced on the  $\text{NO}_3^-$ RR. [11, 12] Another consideration for choosing  $\text{NO}_3^-$  lies in the ever-increasing content of  $\text{NO}_3^-$  in ground water and the great harm to human health. [13] Thus, the  $\text{NO}_3^-$ RR not only provides an ideal route for mass production of  $\text{NH}_3$  under ambient conditions but also helps to solve environmental problems. However, the  $\text{NO}_3^-$ RR involves multiple electrons-coupled protons transfer and various reaction

intermediates, as well as competitive hydrogen evolution reaction (HER), leading to low Faradaic efficiencies towards target  $\text{NH}_3$ . [14] To this end, extensive efforts have been devoted to exploring selective electrocatalysts for the  $\text{NO}_3^-$ RR, and high Faradic efficiencies towards  $\text{NH}_3$  ( $\text{FE}_{\text{NH}_3}$ ) (>90%) have currently achieved on Cu-based electrocatalysts. [9, 15] However, the Cu-catalyzed  $\text{NO}_3^-$ RR usually suffers from sluggish reaction kinetics with great difficulties to achieve large current densities (i.e.,  $200 \text{ mA cm}^{-2}$ ) required for practical applications. [16, 17] Therefore, it is highly desirable to investigate the fundamental origin underlying the sluggish kinetics, aiming at further enhancing the  $\text{NO}_3^-$ RR activity of Cu-based catalysts.

The  $\text{NO}_3^-$ RR in alkaline media ( $\text{NO}_3^- + 6\text{H}_2\text{O} + 8\text{e}^- \rightarrow \text{NH}_3 + 9\text{OH}^-$ ) involves nine proton-coupled electron transfer (PCET). [2, 11] It is well known that protons are produced by the water dissociation under alkaline media. ( $\text{H}_2\text{O} \rightarrow \text{H}^* + \text{OH}^*$ ). [18, 19] To this end, the proton transfer kinetics and reaction kinetics of  $\text{NO}_3^-$ RR are inherently governed by the energy barrier of water dissociation. As it reported, such barrier is really large on metallic Cu [20], most probably resulting in sluggish kinetics of proton transfer for greatly limiting the performance of  $\text{NO}_3^-$ RR. However, most efforts for boosting the  $\text{NO}_3^-$ RR activity of Cu are focused on the regulating the binding energies towards nitrogen-containing intermediates (i.e.,  $^*\text{NO}$ ) [20], and few has done work to investigate how the water dissociation ability and the proton transfer kinetics impact the Cu-catalyzed  $\text{NO}_3^-$ RR.

Yolk-shell nanostructures, with spatially separated core and shell, can avoid the cross-talk between core and shell (i.e., electronic structure changes induced by interfacial interactions), providing great convenience for elucidating the structures-activity relationship and the impacts of proton transfer rate on the performance of  $\text{NO}_3^-$ RR. Herein, we attempt to boost the proton transfer kinetics and consequently the  $\text{NO}_3^-$ RR activity of Cu by creating a yolk-shell structure. We begin with density functional theory (DFT) calculations for searching the Cu-based compounds with strong water dissociation ability, and the results indicate that the  $\text{Cu}_2\text{Se}$  may be the suitable one. Accordingly, we construct a yolk-shell nanostructure, comprising metallic Cu core and  $\text{Cu}_2\text{Se}$  shell that functions like a tandem nanoreactor, in which the proton is generated on the  $\text{Cu}_2\text{Se}$  shell via the water dissociation and then transfers to the Cu core for reacting with  $\text{NO}_3^-$  and following intermediates, thus forming the final product of  $\text{NH}_3$ . By regulating the void size of nanoreactors, the proton flux coming from  $\text{Cu}_2\text{Se}$  shell to the Cu core can be tuned, which in turn controls the coverage of  $\text{H}^*$  intermediates on the surface of Cu for suppressing the HER and promoting the proton transfer of  $\text{NO}_3^-$ RR. As a result, the nanoreactor with an optimized void size of 60 nm displays excellent performance with a  $\text{FE}_{\text{NH}_3}$  of 99.6% and  $\text{NH}_3$  yield rate of  $0.94 \text{ mmol cm}^{-2} \text{ h}^{-1}$  at a potential of -0.15 V vs RHE. This can be attributed to that the suitable coverage of  $\text{H}^*$  on the surface of Cu core promotes the hydrogenation of key intermediates (i.e.,  $^*\text{NO}$  and  $^*\text{NOH}$ ) for reducing the energy barrier of rate-determining step (RDS) in the  $\text{NO}_3^-$ RR, as demonstrated on both results of proton transfer kinetics studies and operando Raman spectra.

## 2. Results And Discussion

Since the metallic Cu has demonstrated good performance for the  $\text{NO}_3^-$ RR[9], we select Cu as core to construct the yolk-shell structure. We note that the water dissociation process on Cu is an endothermic process with large energy requirement[20], which may be adverse to the  $\text{NO}_3^-$ RR. We reason that constructing a shell with good water dissociation ability can accelerate the sluggish proton transfer and reaction kinetics of  $\text{NO}_3^-$ RR on Cu. DFT calculations were then performed on Cu and  $\text{Cu}_2\text{Se}$  to examine their water dissociation ability. (Figure 1a) On the Cu, the water dissociation is an endothermic process with the requirement energy of 0.14 eV, in consistent with other literatures.[20] In sharp contrast, the water dissociation on the  $\text{Cu}_2\text{Se}$  turns to be exothermic with the release energy of 0.47 eV. This suggests that the water dissociation is more favorable on the  $\text{Cu}_2\text{Se}$  than the Cu. Moreover, the adsorption strength of  $\text{H}^*$  is higher on the  $\text{Cu}_2\text{Se}$  than the Cu (Figure 1a), and the too strong adsorption strength makes the  $\text{H}^*$  difficult to achieve the dimerization and generate  $\text{H}_2$  on the  $\text{Cu}_2\text{Se}$  for suppressing the HER.[21, 22] We are grateful to find that the adsorption strength of  $\text{NO}_3^-$  reactants is also much higher on the  $\text{Cu}_2\text{Se}$  than Cu, which can favor the adsorption of  $\text{NO}_3^-$  for promoting the  $\text{NO}_3^-$ RR. (Figure S1) The optimize surface configurations of water, hydrogen, and  $\text{NO}_3^-$  adsorbed on the Cu and  $\text{Cu}_2\text{Se}$  are shown in Figure 1b-1c and S1-S2. With unique features of strong water dissociation ability and strong adsorption strength of both  $\text{H}^*$  and  $\text{NO}_3^-$ , the  $\text{Cu}_2\text{Se}$  may be the suitable one as shell for constructing the yolk-shell structure, thereby boosting the proton transfer and reaction kinetics of  $\text{NO}_3^-$ RR on the Cu core.

As a proof-of-concept study, we constructed the yolk-shell structure comprising the metallic Cu core and  $\text{Cu}_2\text{Se}$  shell (denoted YS-Cu@ $\text{Cu}_2\text{Se}$ ). The YS-Cu@ $\text{Cu}_2\text{Se}$  was then synthesized via the electrochemical reduction of the yolk-shell structure comprising  $\text{Cu}_2\text{O}$  core and  $\text{Cu}_2\text{Se}$  shell (denoted YS- $\text{Cu}_2\text{O}$ @ $\text{Cu}_2\text{Se}$ ). A two-step route was developed to synthesize the YS- $\text{Cu}_2\text{O}$ @ $\text{Cu}_2\text{Se}$ . (Figure 1d) First, uniform  $\text{Cu}_2\text{O}$  nanocubes (denoted  $\text{Cu}_2\text{O}$ -NB) in diameter of 400 nm (Figure S3 and Figure S4) were reacted with NaHSe aqueous solution to generate the core-shell structured  $\text{Cu}_2\text{O}$ @ $\text{Cu}_2\text{Se}$  (denoted CS- $\text{Cu}_2\text{O}$ @ $\text{Cu}_2\text{Se}$ ). Then, the CS- $\text{Cu}_2\text{O}$ @ $\text{Cu}_2\text{Se}$  was treated with an ammonia aqueous solution to etch the  $\text{Cu}_2\text{O}$  core, thereby creating voids between core and shell and thus generating the yolk-shell structured YS- $\text{Cu}_2\text{O}$ @ $\text{Cu}_2\text{Se}$ . As the  $\text{Cu}_2\text{Se}$  shell is not as high activity as  $\text{Cu}_2\text{O}$  in the reaction with ammonia, the shell can be kept after the treatment. To optimize the  $\text{NO}_3^-$ RR performance, the void size of YS- $\text{Cu}_2\text{O}$ @ $\text{Cu}_2\text{Se}$  is continuously regulated by altering the ammonia treatment time.

Transmission electron microscopy (TEM) images of CS- $\text{Cu}_2\text{O}$ @ $\text{Cu}_2\text{Se}$  display a typical core-shell structure with a shell in thickness of  $\sim 19$  nm. (Figure 2a) Corresponding high-resolution TEM (HRTEM) images signify that the shell has continuous lattice fringes with a distance of 0.20 nm, corresponding to (220) plane of  $\text{Cu}_2\text{Se}$ . (Figure S5) Upon treatment of ammonia for 0.5 h, a void in size of 40 nm can be observed between the shell and core. (Figure 2b) With ammonia treatment time gradually increases from 0.5 to 1 and 1.5 h, the size of void enlarges to 60 and 80 nm. (Figure 2c and 2d) These samples after the

treatment were denoted YS-Cu<sub>2</sub>O@Cu<sub>2</sub>Se-40, YS-Cu<sub>2</sub>O@Cu<sub>2</sub>Se-60, and YS-Cu<sub>2</sub>O@Cu<sub>2</sub>Se-80 (40, 60, and 80 stands for the void size). Scanning electron microscopy (SEM) images of sample before and after the treatment are shown in Figure S6, revealing that the treatment makes the smooth surface of shell turn to be rough. This may increase the surface area for exposing more active sites. Since the YS-Cu<sub>2</sub>O@Cu<sub>2</sub>Se-60 displays higher NO<sub>3</sub><sup>-</sup>RR activity than other yolk-shell structure with different void sizes, our attention is focused on this sample. (Figure S7) Energy-dispersive X-ray spectrum (EDX) elemental mapping of YS-Cu<sub>2</sub>O@Cu<sub>2</sub>Se-60 further confirms the successful generation of a yolk-shell structure with a Cu<sub>2</sub>Se shell. (Figure 2e-2g) For comparison, we also completely remove the Cu<sub>2</sub>O core to obtain the hollow structured Cu<sub>2</sub>Se nanoboxes (denoted H-Cu<sub>2</sub>Se) by further extending the treatment time

(Details see experimental section). (Figure S8) X-ray diffraction (XRD) characterizations of H-Cu<sub>2</sub>Se manifest a set of peaks for the Cu<sub>2</sub>Se without other peaks for the Cu<sub>2</sub>O (Figure S9), signifying the complete removal of Cu<sub>2</sub>O core. As for the YS-Cu<sub>2</sub>O@Cu<sub>2</sub>Se-60 with both Cu<sub>2</sub>Se and Cu<sub>2</sub>O, the only presence of peaks for Cu<sub>2</sub>O may be due to the shielding effect of strong Cu<sub>2</sub>O peaks on weak Cu<sub>2</sub>Se ones. (Figure S10)

As it well reported, the Cu<sub>2</sub>O easily transforms to metallic Cu under a reductive potential[23, 24], whereas the Cu<sub>2</sub>Se can resist the reduction even at a highly negative potential of -2.4 V vs Ag/Ag<sup>+</sup> (nearly -1.8 V vs RHE).[25] Inspired by this, we selected a moderate reductive potential (i.e., -0.4 V vs RHE) to electrochemically reduce the Cu<sub>2</sub>O core of YS-Cu<sub>2</sub>O@Cu<sub>2</sub>Se to Cu while remain the crystal phase of Cu<sub>2</sub>Se shell unchanged. In order to avoid the mutual interference of Cu<sub>2</sub>Se core and Cu<sub>2</sub>O shell, their electro-reduction behaviors were investigated separately. After the electro-reduction of Cu<sub>2</sub>O-NBs, strong XRD peaks for metallic Cu are observed instead of those for Cu<sub>2</sub>O phase (Figure S11), indicating that the Cu<sub>2</sub>O has completely transformed to the metallic Cu. Moreover, all peaks for Cu-O bonds are disappeared on the Raman spectra (Figure S12), and X-ray photoelectron spectroscopy (XPS) spectra display only peaks for metallic Cu (Figure S13). By combining the above XRD, Raman and XPS results, it is clear that the electro-reduction enables the complete transformation of Cu<sub>2</sub>O to metallic Cu. However, the electro-reduction does not change the crystal phase of H-Cu<sub>2</sub>Se, and the XRD peaks for Cu<sub>2</sub>Se still dominates after the reduction. (Figure S14) This can be further evidenced by the Raman and XPS spectra. (Figure S15 and S16) Based on the above results, we reason that the Cu<sub>2</sub>O core of YS-Cu<sub>2</sub>O@Cu<sub>2</sub>Se-60 transforms to metallic Cu yet the Cu<sub>2</sub>Se remains its crystal phase. The transformation of Cu<sub>2</sub>O-Cu can be confirmed by the disappearance of both XRD peaks for Cu<sub>2</sub>O after the reduction of YS-Cu<sub>2</sub>O@Cu<sub>2</sub>Se-60. (Figure S17) As for the Cu<sub>2</sub>Se shell, unchanged lattice fingers for the Cu<sub>2</sub>Se are observed, implying that the crystal phase of Cu<sub>2</sub>Se shell remains unchanged after the reduction. (Figure S18) Elemental mapping images of YS-Cu<sub>2</sub>O@Cu<sub>2</sub>Se-60 after the reduction manifest that the yolk-shell structure with a Cu<sub>2</sub>Se shell is well preserved. (Figure S19) Overall, after the electro-reduction, the YS-Cu<sub>2</sub>O@Cu<sub>2</sub>Se-60 successfully converts into the yolk-shell structured nanoreactor composed of a metallic Cu core and a Cu<sub>2</sub>Se shell (denoted YS-Cu@Cu<sub>2</sub>Se-60). In addition, according to the distinct electro-reduction behaviors of Cu<sub>2</sub>O and

Cu<sub>2</sub>Se, the Cu<sub>2</sub>O-NB, CS-Cu<sub>2</sub>O@Cu<sub>2</sub>Se, and H-Cu<sub>2</sub>Se after the reduction are denoted Cu-NB, CS-Cu@Cu<sub>2</sub>Se and H-Cu<sub>2</sub>Se, respectively.

The electrochemical performance of Cu-NB, CS-Cu@Cu<sub>2</sub>Se, YS-Cu@Cu<sub>2</sub>Se-60, and H-Cu<sub>2</sub>Se for the NO<sub>3</sub><sup>-</sup>RR was evaluated in 1 M KOH containing 0.1 M NO<sub>3</sub><sup>-</sup>, and their linear sweeping voltammograms (LSV) curves are shown in Figure 3a. With the shell of Cu<sub>2</sub>Se, the CS-Cu@Cu<sub>2</sub>Se displays higher NO<sub>3</sub><sup>-</sup>RR activity than the Cu-NBs without the shell, indicating that the shell facilitates the NO<sub>3</sub><sup>-</sup>RR. After creating void space to generate the yolk-shell structure, a further large enhancement of NO<sub>3</sub><sup>-</sup>RR activity is achieved on the YS-Cu@Cu<sub>2</sub>Se-60, reflecting that the yolk-shell structure also plays important roles for boosting the NO<sub>3</sub><sup>-</sup>RR. For example, at an applied potential of 0.18 V vs RHE, the YS-Cu@Cu<sub>2</sub>Se-60 yields a current density of 9.6 mA cm<sup>-2</sup>, which is 30- and 2.8-fold larger than the Cu-NB, and CS-Cu@Cu<sub>2</sub>Se, respectively, indicating the much higher intrinsic NO<sub>3</sub><sup>-</sup>RR activity of YS-Cu@Cu<sub>2</sub>Se-60. Impressively, no obvious NO<sub>3</sub><sup>-</sup>RR activity is observed on the YS-Cu@Cu<sub>2</sub>Se-60 after the mass loading is halved, further confirming its good NO<sub>3</sub><sup>-</sup>RR activity. (Figure S20) Moreover, the H-Cu<sub>2</sub>Se is almost inactive for the NO<sub>3</sub><sup>-</sup>RR with negligible current densities, which can be attributed to the too strong adsorption strength of Cu<sub>2</sub>Se towards NO<sub>3</sub><sup>-</sup> (as shown in above DFT calculations) for inhibiting the following reaction processes of NO<sub>3</sub><sup>-</sup>RR. Thus, in the present YS-Cu@Cu<sub>2</sub>Se-60, the metallic Cu core are the genuine active sites for the NO<sub>3</sub><sup>-</sup>RR, and the yolk-shell structure with a Cu<sub>2</sub>Se shell can significantly enhance the activity of Cu.

Liquid products from the NO<sub>3</sub><sup>-</sup>RR were fully analyzed through the ultraviolet-visible (UV-Vis) spectra for determining FE<sub>NH<sub>3</sub></sub>. According to Figure S21-S22, the NH<sub>4</sub><sup>+</sup> cations are the only detected liquid products at different potentials. We then quantified the content of NH<sub>4</sub><sup>+</sup> in liquid products via both UV-Vis and <sup>1</sup>H nuclear magnetic resonance (NMR) spectroscopy (Figure S23). We find that the results of UV-Vis and <sup>1</sup>H NMR match well one with another (Figure S24), reflecting the reliability of our tested NH<sub>4</sub><sup>+</sup> content. The origins of NH<sub>4</sub><sup>+</sup> were studied by performing an isotope tracing experiment. After changing the <sup>14</sup>NO<sub>3</sub><sup>-</sup> to <sup>15</sup>NO<sub>3</sub><sup>-</sup> as reactants, the <sup>1</sup>H NMR of obtained NO<sub>3</sub><sup>-</sup>RR products display two peaks corresponding to <sup>15</sup>NH<sub>4</sub><sup>+</sup> instead of three peaks to <sup>14</sup>NH<sub>4</sub><sup>+</sup>, verifying that the produced NH<sub>4</sub><sup>+</sup> is indeed originated from the NO<sub>3</sub><sup>-</sup>RR other than other impurities.[26] (Figure 3b) Moreover, chromatograms of gas products indicate that the hydrogen (H<sub>2</sub>) is the only product at different potentials without the byproduct of N<sub>2</sub>. (Figure S25)

Combining results of UV-Vis and chromatograms, we calculated the FE<sub>NH<sub>3</sub></sub> at different potentials. (Figure 3c) Obviously, the YS-Cu@Cu<sub>2</sub>Se has good ability for suppressing the competitive HER with high FE<sub>NH<sub>3</sub></sub> values of more than 95% over a wide potential range from -0.05 V to -0.20 V vs RHE. Notably, the YS-Cu@Cu<sub>2</sub>Se delivers a maximum FE<sub>NH<sub>3</sub></sub> up to 99.6% at the potential of -0.15 V vs RHE. Accordingly, at the potential of -0.15 V vs RHE, the YS-Cu@Cu<sub>2</sub>Se achieves a NH<sub>3</sub> yield rate of 0.94 mmol cm<sup>-2</sup> h<sup>-1</sup>, 2.54- and 1.45-fold larger than the Cu-NB, CS-Cu@Cu<sub>2</sub>Se, further corroborating the much higher NO<sub>3</sub><sup>-</sup>RR activity of

YS-Cu@Cu<sub>2</sub>Se-60. (Figure 3d) Impressively, the NH<sub>3</sub> yield rate of YS-Cu@Cu<sub>2</sub>Se-60 (0.94 mmol cm<sup>-2</sup> h<sup>-1</sup>) compares favorably with other reported non-precious electrocatalysts, such as Fe-PPy single-atom (0.16 mmol cm<sup>-2</sup> h<sup>-1</sup>)[27], Cu<sub>50</sub>Ni<sub>50</sub> alloys (0.79 mmol cm<sup>-2</sup> h<sup>-1</sup>)[11], Fe single-atom (0.062 mmol cm<sup>-2</sup> h<sup>-1</sup>) [10], Cu nanosheets (0.023 mmol cm<sup>-2</sup> h<sup>-1</sup>)[28], Porous Cu<sub>70</sub>Ni<sub>30</sub> (0.0026 mmol cm<sup>-2</sup> h<sup>-1</sup>)[17], Copper powders (0.27 mmol cm<sup>-2</sup> h<sup>-1</sup>)[29], and even comparable with some precious-metal-based electrocatalysts, such as Strained Ru Nanoclusters (1.17 mmol cm<sup>-2</sup> h<sup>-1</sup>)[12]. (Figure 3e), demonstrating the great potentials of YS-Cu@Cu<sub>2</sub>Se-60 as electrocatalysts for practical electrosynthesis of NH<sub>3</sub> under mild conditions.

Electrochemically active surface area (ECSA) provides a method to estimate the number of active sites on electrocatalysts.[21, 30, 31] (Figure S26) In general, the ECSA values can be estimated through the double-layer capacitance (C<sub>dl</sub>). The C<sub>dl</sub> value of YS-Cu@Cu<sub>2</sub>Se-60 (9.6 mF cm<sup>-2</sup>) is larger than the Cu-NB (7.6 mF cm<sup>-2</sup>) and CS-Cu@Cu<sub>2</sub>Se (9.0 mF cm<sup>-2</sup>). The larger C<sub>dl</sub> value of YS-Cu@Cu<sub>2</sub>Se-60 implies that the void space of yolk-shell promotes active sites exposure. Moreover, LSV curves, normalized to C<sub>dl</sub> values, reveal that the YS-Cu@Cu<sub>2</sub>Se-60 has higher intrinsic NO<sub>3</sub><sup>-</sup>RR activity than the other two electrocatalysts. (Figure S27) In addition, yolk-shell structured electrocatalysts with a protective shell usually have enhanced stability than the counterpart without.[32] To this end, we tested the stability of YS-Cu@Cu<sub>2</sub>Se-60 by conducting 20-h consecutive NO<sub>3</sub><sup>-</sup>RR. (Figure 3f) During the stability test, the nearly unchanged current density, together with the unchanged FE<sub>NH<sub>3</sub></sub> (Figure S28), signifies the excellent stability of YS-Cu@Cu<sub>2</sub>Se-60 for NO<sub>3</sub><sup>-</sup>RR. Moreover, the well-preserved yolk-shell structure after the stability test further confirms the stable nature of such yolk-shell structure. (Figure S29)

As discussed above, the Cu<sub>2</sub>Se shell may promote the water dissociation to provide protons for boosting the proton transfer and reaction kinetics of NO<sub>3</sub><sup>-</sup>RR on Cu core. To verify it, we performed kinetic isotope effect (KIE) measurements to investigate the proton transfer kinetics of electrocatalysts. As it well reported, KIE values can be obtained according to the following equation:  $KIE = j_D/j_H$ , where  $j_D$  and  $j_H$  stand for the current densities recorded in protic solution and deuterium solution, respectively.[33] Note that the equation hypothesizes that the rate of electrochemical reactions is directly proportional to the tested current density.[34] Accordingly, the equation is applicable only under conditions that the Faradaic efficiency is unchanged in either protonic or deuterium electrolyte. As such, we also tested the FE<sub>NH<sub>3</sub></sub> of Cu-NB and YS-Cu@Cu<sub>2</sub>Se-60 at the potential of -0.15 V vs RHE in a deuterium electrolyte (1 M NaOD in D<sub>2</sub>O). (Figure S30) The nearly unchanged FE<sub>NH<sub>3</sub></sub> after altering the protonic to deuterium electrolyte suggest the availability of the above equation to calculate KIE values of these two electrocatalysts.

KIE values can offer information regarding with the proton transfer kinetics of electrochemical reactions and thus help to understand the rate-determining step (RDS). Generally, a KIE value > 1 signifies that the proton transfer process is existed in the RDS of reactions, however a KIE value ≈ 1 reflects no existence of proton transfer event in the RDS.[35, 36] A large current density decrease is observed on the Cu-NB after

changing the electrolyte from 1 M NaOH/H<sub>2</sub>O to 1 M NaOD/D<sub>2</sub>O (Figure 4a), and the KIE is as large as 4.8, suggesting that the proton transfer process is involved in the RDS of NO<sub>3</sub><sup>-</sup>RR on Cu-NB, and the reaction kinetics is greatly limited by the sluggish proton transfer. In strikingly contrast, the change of electrolyte only induces a slight current density decay on the YS-Cu@Cu<sub>2</sub>Se-60 with a KIE value of 1.3. (Figure 4b) The much smaller KIE value of YS-Cu@Cu<sub>2</sub>Se-60 than the Cu-NB suggests that the sluggish proton transfer of Cu can be indeed enhanced by the yolk-shell structure. The reaction kinetics of these two electrocatalysts were then investigated through determining Tafel slopes. The Tafel slope of YS-Cu@Cu<sub>2</sub>Se-60 is 107.3 mV dec<sup>-1</sup>, smaller than that of Cu-NB (123.9 mV dec<sup>-1</sup>) and CS-Cu@Cu<sub>2</sub>Se (119.0 mV dec<sup>-1</sup>), implying the rapider reaction kinetics of YS-Cu@Cu<sub>2</sub>Se.[37, 38] (Figure S31) Overall, protons provided by Cu<sub>2</sub>Se promote the sluggish proton transfer of Cu and thus enhances the reaction kinetics of NO<sub>3</sub><sup>-</sup>RR.

To deepen our understanding on the tandem reaction process, operando Raman spectra were conducted on the Cu-NB and YS-Cu@Cu<sub>2</sub>Se-60 to monitor reaction intermediates during the NO<sub>3</sub><sup>-</sup>RR. On scanning the potential of 0.2 V vs RHE over the Cu-NB, two Raman bands appear at 818 and 1047 cm<sup>-1</sup> that are assigned to in-situ generated NO<sub>2</sub><sup>\*</sup> intermediates and NO<sub>3</sub><sup>\*</sup> reactants adsorbed on the surface of Cu-NB, respectively.[14] (Figure 4c) Further scanning to the potential of 0.1 V vs RHE manifests two new bands at 1534 and 1590 cm<sup>-1</sup> corresponding to adsorbed \*NOH intermediates and \*NH<sub>3</sub> products[14], respectively, and the intensities of these two bands gradually enhanced during the potential further negatively moves to -0.3 V vs RHE. As it reported, the appearance of \*NOH other than the \*NH<sub>2</sub>O intermediates implies that the NO<sub>3</sub><sup>-</sup>RR undergoes the pathway: NO<sub>3</sub><sup>-</sup> → \*NO<sub>3</sub> → \*NO<sub>2</sub> → \*NO → \*NOH → \*N → \*NH → \*NH<sub>2</sub> → \*NH<sub>3</sub>, and the RDS of this pathway is the reduction of \*NO to \*NOH or the following reduction of \*NOH to \*N with the same energy barrier.[39] Notably, the Raman bands for the \*NOH and \*NH<sub>3</sub> are already observed on the YS-Cu@Cu<sub>2</sub>Se-60 at a highly positive potential of 0.2 V vs RHE, 100 mV-positive than that of Cu-NB. (Figure 4d) This suggests that the energy barrier for accomplishing the transformation of \*NO to \*NOH and \*NOH to \*N is decreased on the YS-Cu@Cu<sub>2</sub>Se-60 with respect to the Cu-NB. In other words, the YS-Cu@Cu<sub>2</sub>Se-60 can reduce the energy barrier for the generation of \*NOH and \*N, which are in the RDS of NO<sub>3</sub><sup>-</sup>RR. This can be further verified by the fact that the stronger intensities of \*NOH and \*NH<sub>3</sub> on the YS-Cu@Cu<sub>2</sub>Se-60 than the Cu-NB at each tested potential. Recent reports indicate that the proton can markedly reduce the energy barrier for the hydrogen of nitrogen-containing intermediates during the NO<sub>3</sub><sup>-</sup>RR, such as the hydrogenation of \*NHO to \*NH<sub>2</sub>O and \*NH<sub>2</sub> to \*NH<sub>3</sub>. [12, 40] Furthermore, our KIE results indicates that the proton transfer is involved in the RDS of NO<sub>3</sub><sup>-</sup>RR, and the Cu<sub>2</sub>Se shell of YS-Cu@Cu<sub>2</sub>Se-60 can provide enough protons to accelerate the proton transfer of NO<sub>3</sub><sup>-</sup>RR, especially the RDS for reducing the energy barrier. This can be evidenced by the smaller apparent energy barrier for the NO<sub>3</sub><sup>-</sup>RR on the YS-Cu@Cu<sub>2</sub>Se-60, compared with the Cu-NBs. (Figure 4e and Figure S32) Thus, we reason that the protons provided by the Cu<sub>2</sub>Se shell promotes the proton transfer of NO<sub>3</sub><sup>-</sup>RR and the

hydrogenation of key intermediates (i.e., \*NO and \*NOH), thereby reducing the energy barrier of RDS step in the NO<sub>3</sub><sup>-</sup>RR. (Figure 4f)

On basis of above comprehensive knowledge of tandem reaction mechanism, we are in a good position to seek a possible explanation on the different NO<sub>3</sub><sup>-</sup>RR activity induced by the geometric alteration of the yolk-shell structure. At first, our electrocatalytic tests are not in static electrolytes but under the stirring of 300 rad/min, and this can eliminate the mass transport limit during the NO<sub>3</sub><sup>-</sup>RR. To verify if the existence of mass transport limit on the yolk-shell structures with different void sizes and Cu-NB, we recorded their LSV curves at different scan rates. All of them display unchanged LSV curves when scan rates are varied, indicating that their mass transport is very rapid without limit.[31, 41] (Figure S33) In other words, the NO<sub>3</sub><sup>-</sup> and OH<sup>-</sup> concentration is the same on the Cu<sub>2</sub>Se shell of different yolk-shell structures, and thus it can assume the proton yield rate on the Cu<sub>2</sub>Se shell is similar at a specific applied potential. Accordingly, the local proton flux arriving to the Cu core varies with the diffusion distance, which is the void size of yolk-shell structure, and obeys the Fick's first law:

$$J = -D \frac{\partial C(x)}{\partial x}$$

where D is the proton diffusion coefficient and can be considered as a constant value for all the YS-Cu@Cu<sub>2</sub>Se-x as the testing conditions are similar to each other.[42, 43] The above equation points out that the proton flux (J) to the Cu core of YS-Cu@Cu<sub>2</sub>Se-x decreases with the void size increases, in the order that YS-Cu@Cu<sub>2</sub>Se-40 > YS-Cu@Cu<sub>2</sub>Se-60 > YS-Cu@Cu<sub>2</sub>Se-80. As for the Cu-NB without the Cu<sub>2</sub>Se shell, the large energy barrier of water dissociation leads to generate limited number of protons and thus enable slow proton transfer rate and the reaction kinetics of NO<sub>3</sub><sup>-</sup>RR. As for the YS-Cu@Cu<sub>2</sub>Se-40 with the Cu<sub>2</sub>Se shell, the small void size confers a high proton flux to Cu core for resulting in high coverage of H\* on the surface of Cu, which is favorable for the formation of H<sub>2</sub> byproducts. (1st panel in Figure 5) This can be evidenced by the higher FE<sub>H<sub>2</sub></sub> of YS-Cu@Cu<sub>2</sub>Se-40 than other two samples. And, the high coverage of H\* would impede the adsorption of nitrogen-containing intermediates and hinder the NO<sub>3</sub><sup>-</sup>RR. It should be noted that the adsorption strength H\* is lower on the Cu than the CuSe<sub>2</sub>, which makes that the H\* is more favorable for the dimerization on the Cu to generate H<sub>2</sub>. With moderate void size, the YS-Cu@Cu<sub>2</sub>Se-60 has suitable H\* coverage on the Cu core surface for enabling rapid proton transfer rate yet hindering the HER. (2nd panel in Figure 5) As for the YS-Cu@Cu<sub>2</sub>Se-80 with largest void size, the small proton flux results in low H\* coverage and thus slow proton transfer rate (3rd panel in Figure 5), which in turn greatly limits the reaction kinetics, in consistent with the lowest NO<sub>3</sub><sup>-</sup>RR of YS-Cu@Cu<sub>2</sub>Se-80 among the three electrocatalysts. Here, we do not discuss the reaction mechanism of CS-Cu@Cu<sub>2</sub>Se because the possible existence of interfacial synergy effect on it makes the reaction mechanism more complex and distinctive with respect to other electrocatalysts. Taken all above results together, it can be concluded that regulating the void size of yolk-shell structured Cu@Cu<sub>2</sub>Se allows to precisely control the H\* coverage on the surface of Cu core for endowing the rapidest proton transfer and reaction kinetics of NO<sub>3</sub><sup>-</sup>RR yet hinder the HER.

### 3. Conclusions

In summary, a yolk-shell structure comprising a Cu core and Cu<sub>2</sub>Se shell has been successfully constructed for highly efficient and selective NO<sub>3</sub><sup>-</sup>RR to generate NH<sub>3</sub>. A set of characterizations indicates that such yolk-shell structure resembles a tandem nanoreactor, in which the Cu<sub>2</sub>Se shell with good water dissociation ability works as a proton producer, and then the protons donate to the Cu core for triggering the NO<sub>3</sub><sup>-</sup>RR. Moreover, the void size of such yolk-shell structure is also tuned to well control the proton flux coming to the Cu core and consequently the \*H coverage on the Cu, thereby allowing rapid proton transfer of NO<sub>3</sub><sup>-</sup>RR yet suppressing HER. Impressively, the optimized yolk-shell structure delivers impressive performance for the NO<sub>3</sub><sup>-</sup>RR, such as an ultrahigh NH<sub>3</sub> yield rate of 0.94 mmol cm<sup>-2</sup> h<sup>-1</sup> at the potential of -0.15 V vs RHE and long-term stability of 20 h, outperforming other reported non-precious electrocatalysts. Mechanism analysis, wherein we integrate the operando characterizations and kinetic isotope studies, reveals that the protons provided by the Cu<sub>2</sub>Se shell can boost the hydrogenation of key intermediates and thus reduce the energy barrier of RDS in the NO<sub>3</sub><sup>-</sup>RR. The above findings not only demonstrate a new methodology to boost the electrochemical NO<sub>3</sub><sup>-</sup>-NH<sub>3</sub> conversion by constructing tandem reactors with tunable yolk-shell structures but also offers deep insights into how the proton transfer rate impacts the reaction kinetics and energy barrier of NO<sub>3</sub><sup>-</sup>RR.

### Declarations

### Acknowledgements

The financial support of the National Natural Science Foundation (NNSF) of China

### References

1. Christensen, C.H. *et al.* Towards an ammonia-mediated hydrogen economy?, *Catal. Today*. **111**, 140–144 (2006).
2. Chen, G.-F. *et al.* Electrochemical reduction of nitrate to ammonia via direct eight-electron transfer using a copper–molecular solid catalyst, *Nat. Energy*. **5**, 605–613(2020).
3. Licht, S. *et al.* Ammonia synthesis by N<sub>2</sub> and steam electrolysis in molten hydroxide suspensions of nanoscale Fe<sub>2</sub>O<sub>3</sub>, *Science* **345**, 637–640(2014).
4. Jin, H. *et al.* Nitrogen Vacancies on 2D Layered W<sub>2</sub>N<sub>3</sub>: A Stable and Efficient Active Site for Nitrogen Reduction Reaction, *Adv. Mater.* **31**, 1902709 (2019).
5. Zhang, L. *et al.* Electrochemical Ammonia Synthesis via Nitrogen Reduction Reaction on a MoS<sub>2</sub> Catalyst: Theoretical and Experimental Studies, *Adv. Mater.* **30**, 1800191(2018).
6. Yao, Y. *et al.* Electrochemical Nitrogen Reduction Reaction on Ruthenium, *ACS Energy Lett* **4**, 1336–1341(2019).

7. Foster, S.L. *et al.* Catalysts for nitrogen reduction to ammonia, *Nat. Catal.* **1**, 490–500(2018).
8. Cheng, H. *et al.* Molybdenum Carbide Nanodots Enable Efficient Electrocatalytic Nitrogen Fixation under Ambient Conditions, *Adv. Mater.* **30**, 1803694(2018).
9. Wang, Y. *et al.* Unveiling the Activity Origin of a Copper-based Electrocatalyst for Selective Nitrate Reduction to Ammonia, *Angew. Chem. Int. Ed.* **59**, 5350–5354(2020).
10. Wu, Z.-Y. *et al.* Electrochemical ammonia synthesis via nitrate reduction on Fe single atom catalyst, *Nat. Commun.* **12**, 2870(2021).
11. Wang, Y. *et al.* Enhanced Nitrate-to-Ammonia Activity on Copper–Nickel Alloys via Tuning of Intermediate Adsorption, *J. Am. Chem. Soc.* **142**, 5702–5708 (2020).
12. Li, J. *et al.* Efficient Ammonia Electrosynthesis from Nitrate on Strained Ruthenium Nanoclusters, *J. Am. Chem. Soc.* **142**, 7036–7046(2020).
13. Garcia-Segura, S. *et al.* Electrocatalytic reduction of nitrate: Fundamentals to full-scale water treatment applications, *Appl. Catal. B Environ.* **236**, 546–568(2018).
14. Butcher, D.P. *et al.* Nitrate reduction pathways on Cu single crystal surfaces: Effect of oxide and Cl<sup>-</sup>, *Nano Energy.* **29**, 457–465 (2016).
15. Mattarozzi, L. *et al.* Electrochemical reduction of nitrate and nitrite in alkaline media at CuNi alloy electrodes, *Electrochim. Acta.* **89**, 488–496 (2013).
16. Comisso, N. *et al.* Electrodeposition of Cu–Rh alloys and their use as cathodes for nitrate reduction, *Electrochem. Commun.* **25**, 91–93(2012).
17. Mattarozzi, L. *et al.* Hydrogen evolution assisted electrodeposition of porous Cu-Ni alloy electrodes and their use for nitrate reduction in alkali, *Electrochim. Acta.* **140**, 337–344(2014).
18. Chen, G. *et al.* Promoted oxygen reduction kinetics on nitrogen-doped hierarchically porous carbon by engineering proton-feeding centers, *Energy Environ. Sci.* **13**, 2849–2855(2020).
19. Zheng, Y. *et al.* The Hydrogen Evolution Reaction in Alkaline Solution: From Theory, Single Crystal Models, to Practical Electrocatalysts, *Angew. Chem. Int. Ed.* **57**, 7568–7579(2018).
20. Luo, M. *et al.* Hydroxide promotes carbon dioxide electroreduction to ethanol on copper via tuning of adsorbed hydrogen, *Nat. Commun.* **10**, 5814(2019).
21. Hu, Q. *et al.* Facile Synthesis of Sub-Nanometric Copper Clusters by Double Confinement Enables Selective Reduction of Carbon Dioxide to Methane, *Angew. Chem. Int. Ed.* **59**, 19054–19059 (2020).
22. Fu, Y. *et al.* Electric Strain in Dual Metal Janus Nanosheets Induces Structural Phase Transition for Efficient Hydrogen Evolution, *Joule* **3**, 2955–2967 (2019).
23. Chang, X. *et al.* pH Dependence of Cu Surface Speciation in the Electrochemical CO Reduction Reaction, *ACS Catal.* **10**, 13737–13747 (2020).
24. Gao, J. *et al.* Selective C–C Coupling in Carbon Dioxide Electroreduction via Efficient Spillover of Intermediates As Supported by Operando Raman Spectroscopy, *J. Am. Chem. Soc.* **141**, 18704–18714(2019).

25. Yang, D. *et al.* Selective electroreduction of carbon dioxide to methanol on copper selenide nanocatalysts, *Nat. Commun.* **10**, 677(2019).
26. Zhang, L. *et al.* Ammonia Synthesis Under Ambient Conditions: Selective Electroreduction of Dinitrogen to Ammonia on Black Phosphorus Nanosheets, *Angew. Chem. Int. Ed.* **58**, 2612–2616(2019).
27. Li, P. *et al.* A single-site iron catalyst with preoccupied active centers that achieves selective ammonia electrosynthesis from nitrate, *Energy Environ. Sci.* **14**, 3522–3531(2021).
28. Fu, X. *et al.* Alternative route for electrochemical ammonia synthesis by reduction of nitrate on copper nanosheets, *Appl. Mater. Today.* **19**, 100620 (2020).
29. Reyter, D. *et al.* Electrocatalytic reduction of nitrate on copper electrodes prepared by high-energy ball milling, *J. Electroanal. Chem.* **596**, 13–24(2006).
30. Hu, Q. *et al.* Superhydrophilic Phytic-Acid-Doped Conductive Hydrogels as Metal-Free and Binder-Free Electrocatalysts for Efficient Water Oxidation, *Angew. Chem. Int. Ed.* **58**, 4318–4322 (2019).
31. Hu, Q. *et al.* A unique space confined strategy to construct defective metal oxides within porous nanofibers for electrocatalysis, *Energy Environ. Sci.* **13**, 5097–5103(2020).
32. Tian, H. *et al.* Nanoengineering Carbon Spheres as Nanoreactors for Sustainable Energy Applications, *Adv. Mater.* **31**, 1903886(2019).
33. Li, W. *et al.* A bio-inspired coordination polymer as outstanding water oxidation catalyst via second coordination sphere engineering, *Nat. Commun.* **10**, 5074(2019).
34. Khadka, N. *et al.* Mechanism of Nitrogenase H<sub>2</sub> Formation by Metal-Hydride Protonation Probed by Mediated Electrocatalysis and H/D Isotope Effects, *J. Am. Chem. Soc.* **139**, 13518–13524 (2017).
35. Liu, Y. *et al.* Modulating the mechanism of electrocatalytic CO<sub>2</sub> reduction by cobalt phthalocyanine through polymer coordination and encapsulation, *Nat. Commun.* **10**, 1683 (2019).
36. Sawata, S. *et al.* Kinetic evidence based on solvent isotope effects for the nonexistence of a proton-transfer process in reactions catalyzed by a hammerhead ribozyme: Implication to the double-metal-ion mechanism of catalysis, *J. Am. Chem. Soc.* **117**, 2357–2358 (1995).
37. Hu, Q. *et al.* Crafting MoC<sub>2</sub>-doped bimetallic alloy nanoparticles encapsulated within N-doped graphene as roust bifunctional electrocatalysts for overall water splitting, *Nano Energy.* **50**, 212–219(2018).
38. Hu, Q. *et al.* Unconventionally fabricating defect-rich NiO nanoparticles within ultrathin metal–organic framework nanosheets to enable high-output oxygen evolution, *J. Mater. Chem. A.* **8**, 2140–2146(2020).
39. Wang, Y. *et al.* First-principles mechanistic study on nitrate reduction reactions on copper surfaces: Effects of crystal facets and pH, *J. Catal.* **400**, 62–70(2021).
40. Deng, X. *et al.* Metallic Co Nanoarray Catalyzes Selective NH<sub>3</sub> Production from Electrochemical Nitrate Reduction at Current Densities Exceeding 2 A cm<sup>-2</sup>, *Adv. Sci.* **8**, 2004523(2021).

41. Song, F. *et al.* Ultrathin Cobalt–Manganese Layered Double Hydroxide Is an Efficient Oxygen Evolution Catalyst, *J. Am. Chem. Soc.* **136**, 16481–16484(2014).
42. Xiong, L. *et al.* Geometric Modulation of Local CO Flux in Ag@Cu<sub>2</sub>O Nanoreactors for Steering the CO<sub>2</sub>RR Pathway toward High-Efficacy Methane Production, *Adv. Mater.* **33**, 2101741(2021).
43. Shi, R. *et al.* Efficient wettability-controlled electroreduction of CO<sub>2</sub> to CO at Au/C interfaces, *Nat. Commun.* **11**, 3028(2020).

## Figures

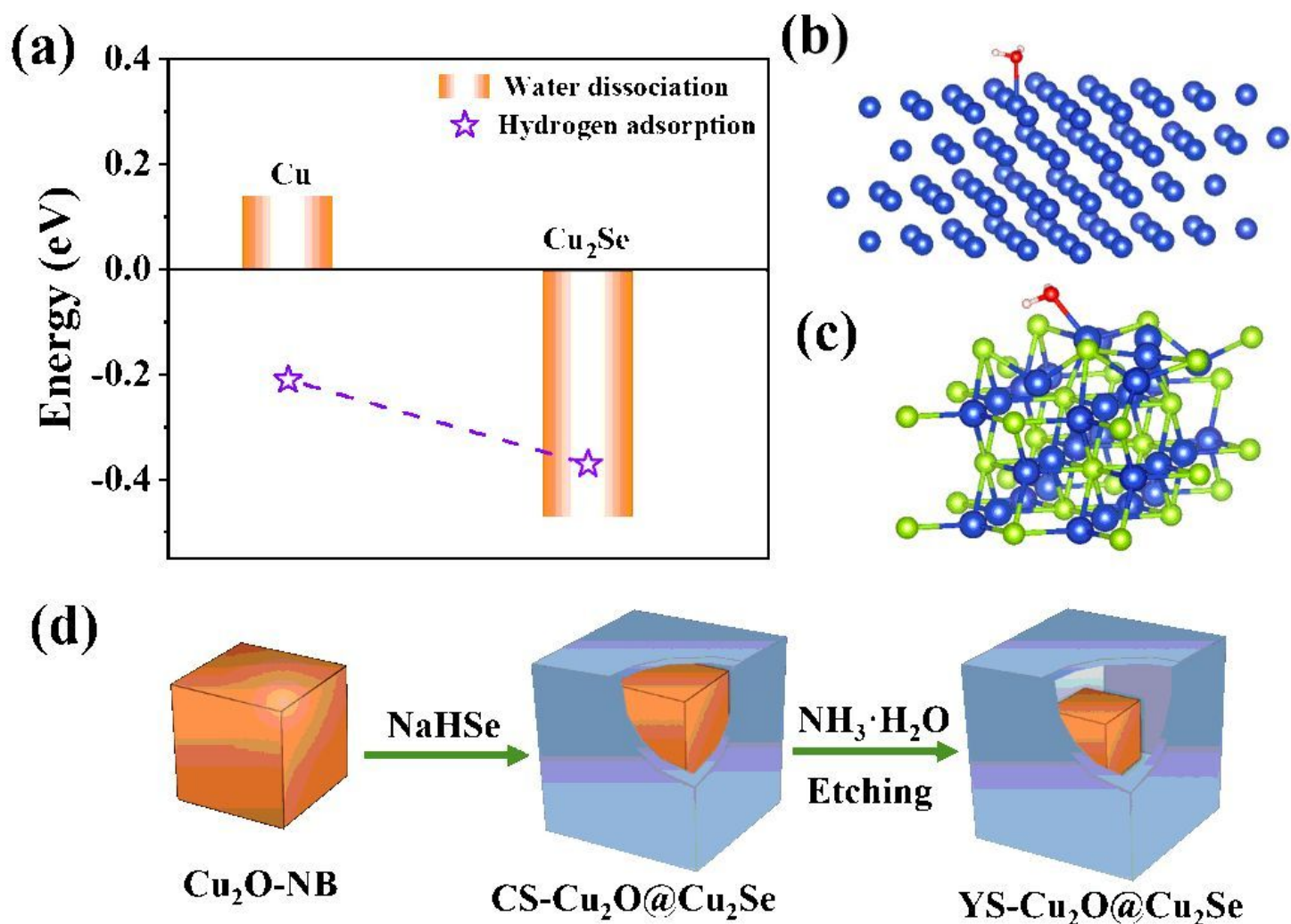
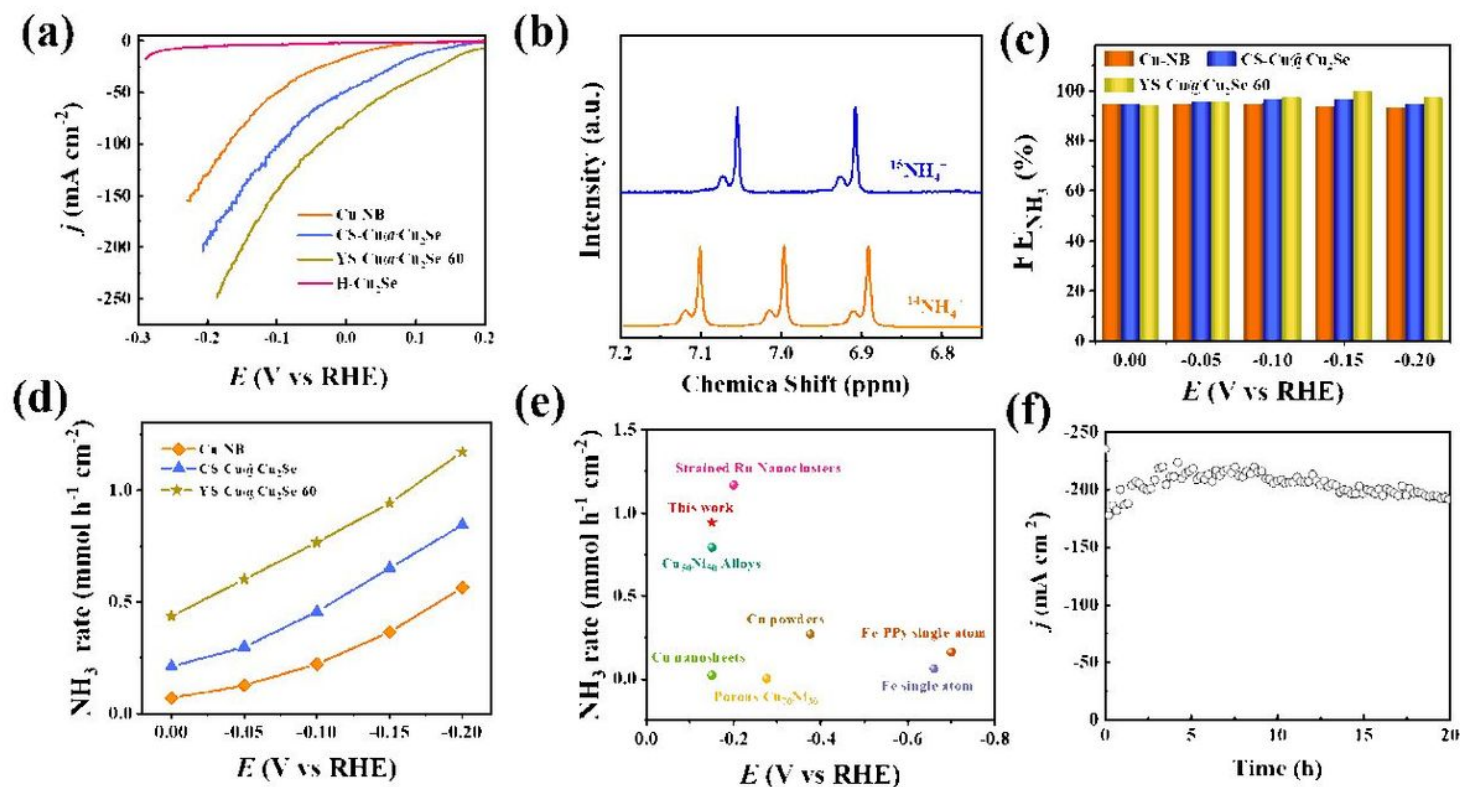


Figure 1

(a) Calculated energies of water dissociation and hydrogen adsorption on the surface of Cu and Cu<sub>2</sub>Se. Optimized surface configurations of water adsorbed on the (b) Cu and (c) Cu<sub>2</sub>Se. (d) Schematic illustration the synthetic process of YS-Cu<sub>2</sub>O@Cu<sub>2</sub>Se, during which the Cu<sub>2</sub>O nanocubes are first reacted with NaHSe to generate the core-shell structured Cu<sub>2</sub>O@Cu<sub>2</sub>Se (CS-Cu<sub>2</sub>O@Cu<sub>2</sub>Se), followed by the



transmission electron microscopy (HADDF-STEM) images of CS-Cu<sub>20</sub>@Cu<sub>2</sub>Se-60 and corresponding elemental mapping of (f) Cu and (g) Se.



**Figure 3**

(a) LSV of Cu-NB, CS-Cu@Cu<sub>2</sub>Se, YS-Cu@Cu<sub>2</sub>Se-60, and H-Cu<sub>2</sub>Se in 1 M KOH with 0.1 M NO<sub>3</sub><sup>-</sup>. (b) <sup>1</sup>H NMR spectra of liquid products obtained from NO<sub>3</sub>-RR using <sup>14</sup>N nitrate and <sup>15</sup>N nitrate as reactants. (c) FE-NH<sub>3</sub>, and (d) NH<sub>3</sub> yield rate of Cu-NB, CS-Cu@Cu<sub>2</sub>Se, and YS-Cu@Cu<sub>2</sub>Se-60. (e) Comparing the NH<sub>3</sub> yield rate of our YS-Cu@Cu<sub>2</sub>Se-60 with other reported electrocatalysts. (f) Stability test of YS-Cu@Cu<sub>2</sub>Se-60 at the potential of -0.15 V vs RHE for 20 h.

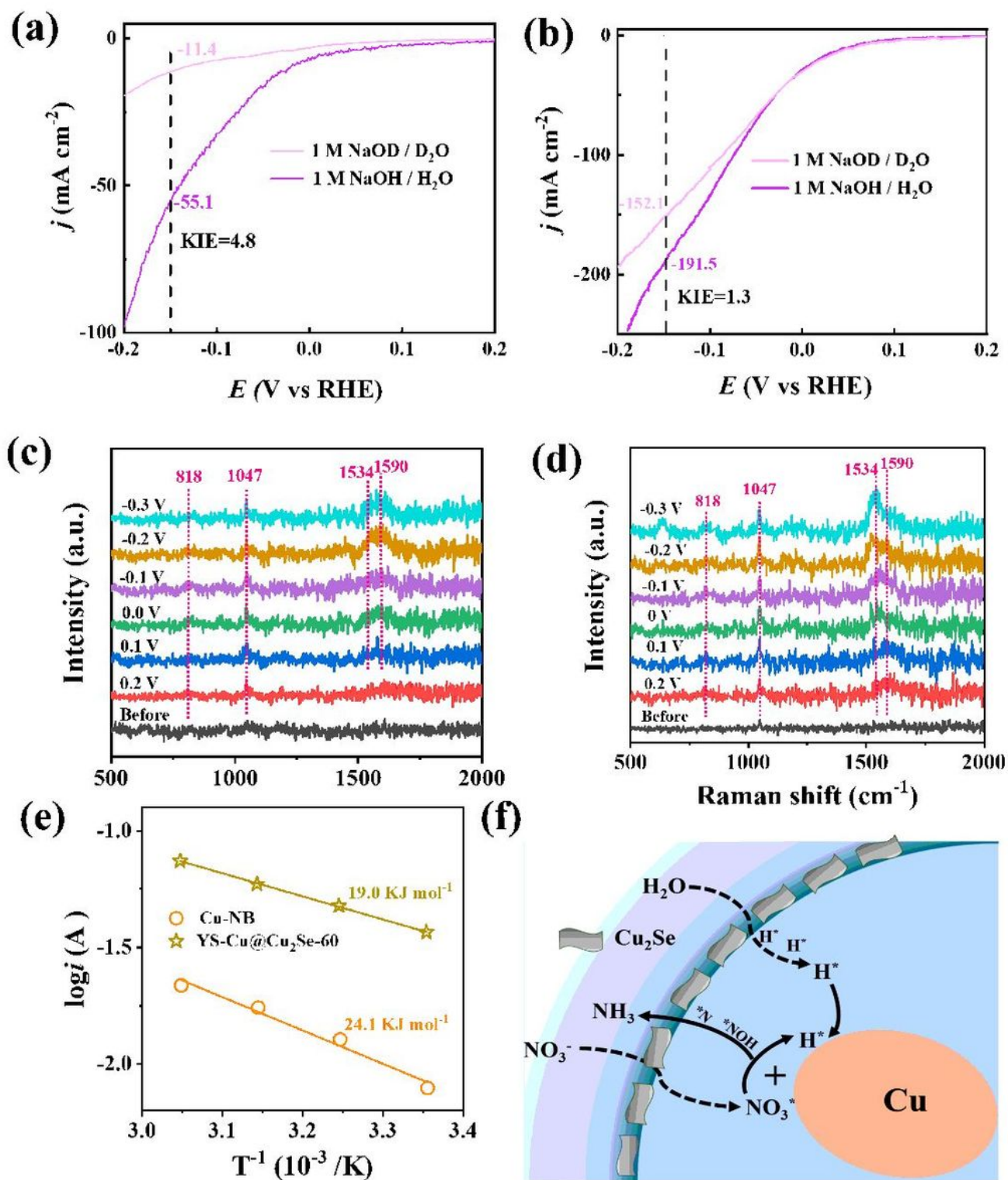


**Figure 4**

(a) Cu-NB, and (b) YS-Cu@Cu<sub>2</sub>Se-60 in 1 M NaOH/H<sub>2</sub>O and 1 M NaOD/D<sub>2</sub>O containing 0.1 M NO<sub>3</sub><sup>-</sup>. (c) Operando Raman spectra recorded at different potentials for the (c) Cu-NB and (d) YS-Cu@Cu<sub>2</sub>Se-60 in the media of 1 M KOH containing 0.1 M NO<sub>3</sub><sup>-</sup>. (e) Arrhenius plots of the NO<sub>3</sub>-RR kinetic current on the Cu-NB and YS-Cu@Cu<sub>2</sub>Se-60 at the potential of -0.05 V vs RHE. (f) Schematic illustration that the yolk-shell structured Cu@Cu<sub>2</sub>Se resembles a tandem nanoreactor, in which the proton is generated on the Cu<sub>2</sub>Se

shell via the water dissociation and then transfers to the Cu core for reacting with  $\text{NO}_3^-$  and following intermediates and thus forming the final product of  $\text{NH}_3$ .

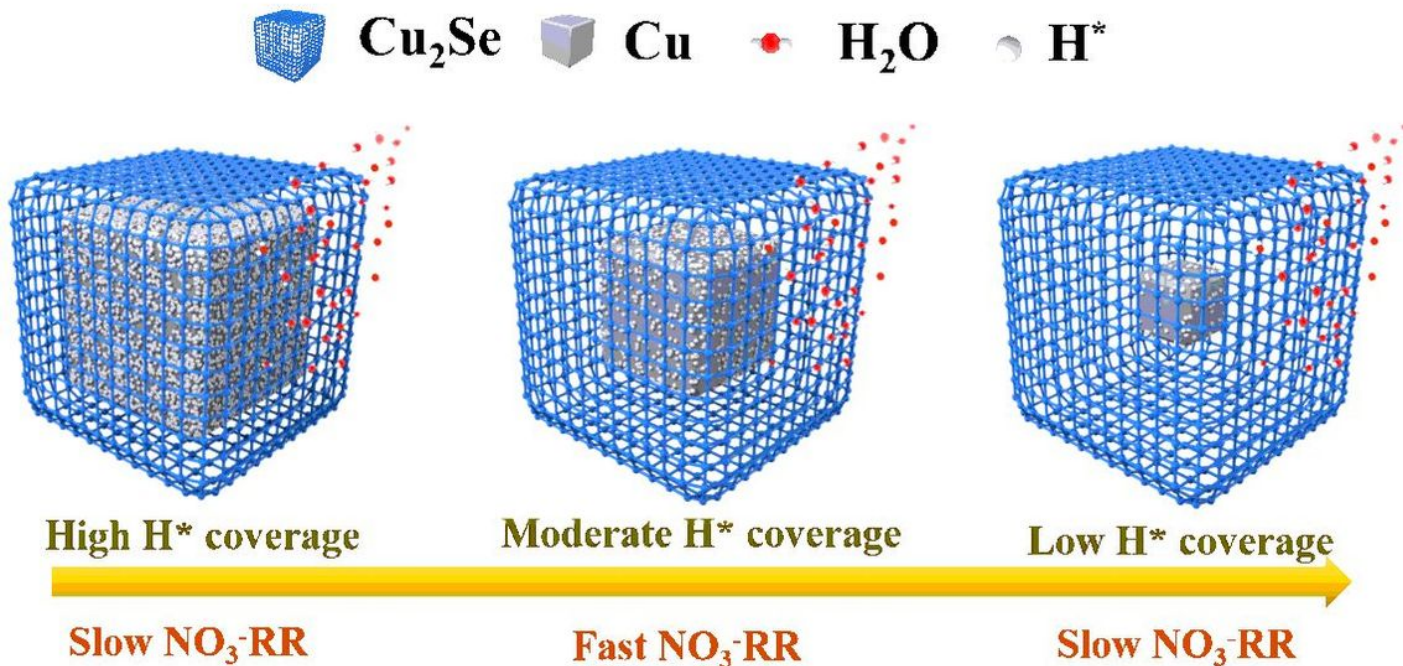


**Figure 5**

Schematic diagrams displaying the proton flux in yolk-shell structured  $\text{Cu}@\text{Cu}_2\text{Se}_x$  with varying void sizes, and the regulation of the  $\text{NO}_3^-$ -RR performance by the different proton flux.

## Supplementary Files

This is a list of supplementary files associated with this preprint. Click to download.

- [Sl.docx](#)